Instantaneous Linkages between Clouds and Large-Scale Meteorology over the Southern Ocean in Observations and a Climate Model

CASEY J. WALL AND DENNIS L. HARTMANN

Department of Atmospheric Sciences, University of Washington, Seattle, Washington

PO-LUN MA

Atmospheric Sciences and Global Change Division, Pacific Northwest National Laboratory, Richland, Washington

(Manuscript received 9 March 2017, in final form 11 August 2017)

ABSTRACT

Instantaneous, coincident, footprint-level satellite observations of cloud properties and radiation taken during austral summer over the Southern Ocean are used to study relationships between clouds and large-scale meteorology. Cloud properties are very sensitive to the strength of vertical motion in the midtroposphere, and low-cloud properties are sensitive to estimated inversion strength, low-level temperature advection, and sea surface temperature. These relationships are quantified. An index for the meteorological anomalies associated with midlatitude cyclones is presented, and it is used to reveal the sensitivity of clouds to the meteorology within the warm and cold sectors of cyclones.

The observed relationships between clouds and meteorology are compared to those in the Community Atmosphere Model, version 5 (CAM5), using satellite simulators. Low clouds simulated by CAM5 are too few, are too bright, and contain too much ice. In the cold sector of cyclones, the low clouds are also too sensitive to variations in the meteorology. When CAM5 is coupled with an updated boundary layer parameterization known as Cloud Layers Unified by Binormals (CLUBB), bias in the ice content of low clouds is dramatically reduced. More generally, this study demonstrates that examining the instantaneous time scale is a powerful approach to understanding the physical processes that control clouds and how they are represented in climate models. Such an evaluation goes beyond the cloud climatology and exposes model bias under various meteorological conditions.

1. Introduction

Clouds play a fundamental role in Earth's energy budget. They reflect incoming shortwave (SW) radiation and reduce the emission of longwave (LW) radiation to space. Because of the strong radiative impact of clouds, and because of their complexity, cloud feedback is the largest source of uncertainty in model projections of global climate change (e.g., Cess et al. 1990; Boucher et al. 2013). Describing clouds in the observational record is important for understanding the energy budget in the present climate and an important first step toward constraining climate change projections.

Clouds and their radiative effects are often poorly simulated by global climate models (GCMs)—especially over the Southern Ocean. Model bias in absorbed SW radiation can be as large as $\pm 30\,\mathrm{W\,m^{-2}}$ over the Southern Ocean, with most models absorbing too much SW radiation (Trenberth and Fasullo 2010; Ceppi et al. 2012). These cloud biases cause large-scale heat transport and circulation biases, both in the atmosphere and in the ocean and both locally and in the tropics (Ceppi et al. 2012; Hwang and Frierson 2013; Kay et al. 2016). Additionally, most models simulate brighter Southern Ocean clouds in response to anthropogenic climate change (Zelinka and Hartmann 2012), and this cloud feedback is thought to drive the large-scale atmospheric circulation response in the Southern Hemisphere extratropics (Voigt and Shaw 2015; Ceppi and Hartmann 2016). Since Southern Ocean clouds are poorly simulated by GCMs, and since they have far-reaching impacts on the climatology and climate change response in GCMs, better understanding of Southern Ocean clouds is needed.

Corresponding author: Casey J. Wall, caseyw8@atmos.washington.edu

DOI: 10.1175/JCLI-D-17-0156.1

The characteristics of Southern Ocean clouds and their connections to the large-scale meteorology can be illuminated by focusing on the instantaneous time scale. The instantaneous time scale is key because time averaging can blend different cloud and meteorological regimes together, thereby obscuring the physical processes that control clouds. Time averaging can also mask compensating model biases, which could cause a model to have a realistic time-mean cloud radiative effect but not necessarily a realistic cloud feedback under anthropogenic forcing. Examining cloud variability on the instantaneous time scale provides a more stringent evaluation of models. For such an evaluation, models perform well only if they simulate realistic cloud regimes with realistic radiative properties, and under the right meteorological conditions.

One common approach to characterize cloud variability and connections to the large-scale meteorology on short time scales is classifying clouds into regimes. This is often done using cluster analysis of observations from the International Satellite Cloud Climatology Project (ISCCP; Rossow and Schiffer 1991) (e.g., Jakob and Tselioudis 2003; Jakob et al. 2005; Rossow et al. 2005; Oreopoulos and Rossow 2011). Using this technique, Gordon and Norris (2010) identified seven cloud regimes over midlatitude oceans that occur in distinct large-scale meteorological conditions. Haynes et al. (2011) quantified the radiative effects of cloud regimes over the Southern Ocean and found that, because they are so common, the low-cloud regimes make the largest contribution to the SW cloud radiative effect. Bodas-Salcedo et al. (2014) quantified climate model bias in reflected SW radiation for the various cloud regimes.

Another approach to characterize cloud variability and connections to the large-scale meteorology on short time scales involves compositing observations based on proximity to the center of midlatitude cyclones (e.g., Lau and Crane 1995, 1997; Norris and Iacobellis 2005; Catto 2016, and references therein). Using this approach, Field and Wood (2007) highlighted the distinct cloud types that exist in cyclones and examined the sensitivity of cloud properties to variations in cyclone strength and atmospheric moisture. Naud et al. (2010) and Govekar et al. (2011) described the vertical distribution of clouds around midlatitude cyclones using active, satellite-based retrievals. Bodas-Salcedo et al. (2014) found that, over the Southern Ocean, climate model bias in reflected SW radiation is dominated by clouds in the cold sector of cyclones.

Cloud regime classification and cyclone compositing have led to major advances in our understanding of Southern Ocean clouds, but both techniques have limitations. Cloud regime classification is limited by the quality of the ISCCP observations, since ISCCP suffers from errors common to passive retrievals. ISCCP performs poorly when multilayered clouds are present and often reports a cloud-top pressure between the multiple cloud layers (Marchand et al. 2010). This is problematic over the Southern Ocean where multilayered clouds are present in roughly one-third of cloudy scenes (Haynes et al. 2011). As a result, layered clouds are often misclassified into ''midlevel'' cloud regimes (Bodas-Salcedo et al. 2014; Mason et al. 2014). Additionally, cyclone compositing has limitations that result from averaging different cyclones together. Cyclones evolve rapidly and are highly variable in their structure and features. Therefore, averaging across different cyclones at different stages of development can result in the loss of information about the large-scale meteorological conditions and their influence on clouds.

In this work we aim to build on the insights from previous studies and further characterize instantaneous linkages between Southern Ocean clouds and the large-scale meteorology. We examine the sensitivity of clouds to variations in four predictors derived from the large-scale meteorology: sea surface temperature (SST), vertical motion in the middle troposphere, estimated inversion strength (Wood and Bretherton 2006), and low-level temperature advection. Each predictor is a proxy for a physical process that impacts clouds. Sea surface temperature is closely related to the surface latent heat flux, and as a result, cooler temperatures favor a shallow and well-mixed boundary layer while warmer temperatures favor a decoupled boundary layer (Bretherton and Wyant 1997). Vertical motion is strongly related to the advective tendency of cloud water mixing ratio. Inversion strength is a proxy for entrainment efficiency: weaker inversions allow for stronger entrainment of dry air from the free troposphere into the boundary layer. Finally, low-level temperature advection influences the stratification and mixing within the boundary layer. Cold advection causes weak stratification and enhanced turbulent mixing, and vice versa. We examine the sensitivity of clouds to each of these processes individually and examine how these processes and clouds vary within midlatitude cyclones.

Our approach provides new insight for two reasons: 1) We use high-quality satellite observations of clouds and radiation from multiple instruments. We use a combination of passive and active retrievals and take advantage of the strengths of each. 2) We composite observations by various meteorological predictors rather than by location with respect to the cyclone center. When compared to cyclone compositing, our approach retains more information about the large-scale meteorological conditions and their influence on clouds.

This study is organized as follows: observational datasets, model simulations, and statistical methods are described in section 2; instantaneous linkages between large-scale meteorological conditions and cloud properties are described in section 3; and conclusions and a summary of the findings are presented in section 4.

2. Data and methods

a. Observational data

We use satellite observations of cloud properties and radiation from the combined CERES-*CloudSat-CALIPSO*-MODIS (CCCM) dataset, version RelB1 (Kato et al. 2010; Loeb et al. 2016). This dataset is a collection of instantaneous, coincident, footprint-level measurements from four instruments based on satellites flying in the A-Train constellation (Stephens et al. 2002). The CERES (Wielicki et al. 1996) instrument retrieves top-of-atmosphere radiative fluxes (Loeb et al. 2005). The Cloud Profiling Radar (CPR; Stephens et al. 2008) on board the *CloudSat* satellite and the Cloud–Aerosol Lidar with Orthogonal Polarization (CALIOP; Winker et al. 2007) on board the *Cloud-Aerosol lidar and Infrared Pathfinder Satellite Observations* (*CALIPSO*) satellite are both active instruments that retrieve the vertical distribution of clouds. The Moderate Resolution Imaging Spectroradiometer (MODIS; [Minnis et al. 2011a]) instrument is a passive imager that retrieves vertically integrated and cloud-top properties. We use observations from all four instruments and take advantage of the strengths of each.

Since the CERES, CPR, CALIOP, and MODIS instruments have different footprint sizes and viewing angles, a minimal amount of averaging and subsetting is done to get the data on a common grid. First, since CPR and CALIOP are nadir-viewing instruments, only near-nadir scenes from CERES and MODIS are used. Second, because CERES has the largest footprint of the four instruments—about 20-km horizontal resolution at nadir—all measurements from other instruments are horizontally averaged across the CERES footprint. A typical CERES footprint contains about 1200 MODIS pixels, 100 CALIOP profiles, and 30 CPR profiles. The MODIS measurements cover nearly the entire CERES footprint, while the CPR and CALIOP instruments view only a ''stripe'' through the middle of the CERES footprint. Finally, CPR and CALIOP profiles are merged to a common vertical grid with 240-m resolution.

We use observations of the vertical profile of cloud fraction from the merged CALIOP–CPR product; albedo and outgoing LW radiation at the top of the atmosphere from CERES; and horizontal cloud fraction and in-cloud (i.e., computed using cloudy pixels only) optical depth, liquid water path (LWP), and ice water path (IWP) from MODIS. Liquid water path is defined as the total mass of cloud liquid water above a unit area of Earth's surface, and similarly for ice water path. The cloud fraction observed by MODIS is a measure of the horizontal coverage of clouds, while the cloud fraction from the CALIOP–CPR product is a measure of the vertical distribution of clouds. We analyze data from December 2006 through February 2011 and restrict our study to latitudes between 40° and 60°S and to the summer months of December, January, and February—months when the absorbed SW bias in climate models is largest. The albedo, optical depth, liquid water path, and ice water path measurements are only available for sunlit scenes. The CCCM variables used in this study are listed in Table 1.

b. Reanalysis data

We also use meteorological variables from the European Centre for Medium-Range Weather Forecasts interim reanalysis (ERA-Interim; Dee et al. 2011; ECMWF 2015). SST, vertical pressure velocity at 500 hPa (ω_{500}), estimated inversion strength (EIS; Wood and Bretherton 2006), and low-level temperature advection are used as meteorological predictor variables. Low-level temperature advection is defined as $-\mathbf{u}_{1000\,\mathrm{hPa}} \cdot \nabla \mathrm{SST}$, where $\mathbf{u}_{1000\,\mathrm{hPa}}$ is the horizontal wind at 1000 hPa. A negative sign is used in this definition so that positive values of low-level temperature advection correspond to warm advection, and vice versa. We also use vertical profiles of temperature, wind, and horizontal temperature advection, which is defined similarly to low-level temperature advection but computed throughout the troposphere. The dataset includes instantaneous realizations of the meteorological fields every six hours with $0.75° \times 0.75°$ horizontal resolution. Meteorological variables are linearly interpolated to the location and time of each satellite footprint.

c. Observational uncertainties

We begin by discussing sampling limitations. Since the A-Train follows a sun-synchronous orbit, and since only near-nadir scenes are included in the CCCM dataset, all scenes from latitude bands are sampled at about the same local time. This has two important consequences. First, all sunlit scenes have solar zenith angles less than 60° and hence are not affected by retrieval biases that occur at large solar zenith angles (Grosvenor and Wood 2014). Second, the diurnal cycle is poorly sampled in the CCCM dataset. Fortunately, the diurnal cycles of cloud fraction and optical depth are small over extratropical oceans (Warren et al. 1988; Rossow and Schiffer 1999),

TABLE 1. Variables from the CCCM dataset and satellite simulators used in this study. The CCCM dataset also includes variables from the CERES single scanner footprint (SSF) dataset. SSF-81, SSF-83, SSF-89, and SSF-91 are MODIS-observed cloud properties averaged over the entire CERES footprint (referred to as "full footprint" in CCCM).

CCCM dataset (observations)	
Variable	Name
SSF-1	Time of observation
SSF-6	Colatitude of subsatellite point at surface at observation
SSF-7	Longitude of subsatellite point at surface at observation
SSF-21	CERES solar zenith at surface
SSF-25	Surface type index
SSF-38	CERES SW TOA flux—upward
SSF-38a	CERES SW TOA flux—downward
SSF-39	CERES LW TOA flux—upward
SSF-81	Clear/layer/overlap percent coverages
SSF-83	Mean visible optical depth for cloud layer
SSF-89	Mean liquid water path for cloud layer (3.7)
SSF-91	Mean ice water path for cloud layer (3.7)
CCCM-52	Cloud fraction profile
CCCM-73	*CloudSat* cloud type histogram
COSP Satellite Simulators	
Variable	Description
CFAD_DBZE94_CS	*CloudSat* radar reflectivity factor
CLD_CAL	*CALIPSO* lidar cloud fraction
CLTMODIS	MODIS total cloud fraction
IWPMODIS	MODIS cloud ice water path
LWPMODIS	MODIS cloud liquid water path
TAUTMODIS	MODIS total cloud optical thickness

so the sampling of CCCM is representative of the climate over the Southern Ocean.

Additionally, each instrument has unique strengths and weaknesses. The main strength of the active instruments is their ability to accurately measure cloud vertical distribution for a wide variety of cloud types. CALIOP can detect thin clouds with optical depths as low as 0.01 (McGill et al. 2007) but becomes fully attenuated at optical depths of about 3 (Winker et al. 2007). As a result, CALIOP often only views the top portion of clouds (Cesana et al. 2016). Compared to CALIOP, the CPR instrument can view deeper into clouds but misses optically thin clouds. The CPR signal can also become fully attenuated during heavy precipitation. The combined CALIOP–CPR cloud fraction is computed using only the scenes where at least one of the instruments made a valid retrieval; when the signal from both instruments is fully attenuated at a certain level, then that measurement is treated as missing data and is excluded from the calculation of cloud fraction. The CPR and CALIOP instruments work synergistically to provide the best global-scale view of cloud vertical structure that is currently available.

Strengths of the CERES instrument include very stable performance over the period of study (Corbett and Loeb 2015) and the ability to make highly accurate retrievals of emitted and reflected radiative fluxes. CERES measures broadband radiances at the top of the atmosphere and uses these measurements to estimate radiative fluxes. Biases introduced in the radiance-to-flux conversion are small and are independent of cloud properties. CERES retrievals of radiative fluxes are consistent across satellite platforms and with independent retrievals from geostationary satellites, lending to their credibility (Loeb et al. 2003).

Uncertainty in cloud properties retrieved by MODIS deserves special attention. MODIS retrieves cloud thermodynamic phase, particle size, and optical depth and then computes the liquid or ice water path from these quantities (Minnis et al. 2011a). MODIS retrievals of cloud-top thermodynamic phase over the Southern Ocean agree quite well with coincident retrievals from CALIOP (Huang et al. 2016), so cloud-top phase determination is not the main source of uncertainty in the MODIS cloud retrievals. Rather, the main source of uncertainty is due to the fact that MODIS views only the highest clouds. The retrieved cloud phase and particle size reflect conditions near the top of the highest clouds (Nakajima and King 1990) but are assumed to be uniform throughout the cloud. This is especially problematic for liquid clouds, since MODIS cannot detect liquid cloud below moderately thick ice cloud. As a result,

when thick or layered clouds are present, liquid cloud properties are usually not retrieved. This is a serious limitation.

To assess the uncertainty in liquid water path retrieved by MODIS, we compared MODIS data to liquid water path retrieved by the Advanced Microwave Scanning Radiometer for EOS (AMSR-E; Wentz and Meissner 2004). AMSR-E also flies in the A-Train, but its retrieval is based on independent physics, uses measurements at different wavelengths, and provides an independent estimate of liquid water path. We examined three months of instantaneous, footprint-level measurements taken over the Southern Ocean by the two instruments and conditionally sampled the data based on vertical motion in the middle troposphere. Differences between AMSR-E and MODIS estimates of liquid water path are small ($10\,g\,m^{-2}$ or less) during large-scale subsidence and large (up to $100\,g\,m^{-2}$) during large-scale ascent (not shown). Both the AMSR-E and MODIS retrievals have large uncertainties when measuring deep, precipitating clouds, so disagreement between the retrievals is expected (Lebsock and Su 2014). From the MODIS and AMSR-E comparison, we conclude that liquid water path retrievals from MODIS are reliable during large-scale subsidence and very uncertain during strong large-scale ascent.

Additionally, Minnis et al. (2011b) compared the MODIS cloud retrievals to measurements from several independent satellite- and surface-based instruments. They generally find good agreement between MODIS and the various datasets. One exception is that optical depth of thin cirrus tends to be underestimated by MODIS compared to surface-based radar retrievals.

d. CAM5

We run simulations with the Community Atmosphere Model, version 5 (CAM5; Neale et al. 2011)—the atmosphere component of a global climate model. CAM5 is run in default configuration and with an updated boundary layer parameterization called Cloud Layers Unified by Binormals (CLUBB; Golaz et al. 2002). These configurations will be referred to as ''CAM5'' and ''CAM5 + CLUBB,'' respectively. CAM5 uses several parameterizations to represent cloud processes, including cloud microphysics (Morrison and Gettelman 2008), cloud macrophysics (Park et al. 2014), shallow convection (Park and Bretherton 2009), deep convection (Zhang and McFarlane 1995), and turbulent mixing (Bretherton and Park 2009). In CAM5 + CLUBB, the cloud macrophysics, shallow convection, and turbulent mixing schemes are replaced by CLUBB, which treats these processes in a unified and consistent framework. CLUBB predicts the distribution of turbulent updrafts and downdrafts, allowing it to simulate a wide range of cloud regimes from stratiform clouds, which occur when the distribution is symmetric, to shallow cumulus clouds, which occur when the distribution is highly skewed. Preliminary evaluations show that CLUBB substantially improves subtropical low clouds simulated by the Community Atmosphere Model (Bogenschutz et al. 2012, 2013). We will continue the evaluation of clouds in CAM5 + CLUBB and examine clouds over the Southern Ocean.

Model simulations are run with sea ice concentration and sea surface temperature prescribed to observed values following the Atmosphere Model Intercomparison Project (AMIP) protocol (Gates 1992), and instantaneous model fields are produced every six hours. We run simulations from 2000 to 2005 and compare the output with observations from 2006 to 2011. Differences between model output and observations are mostly due to model bias rather than differences in the surface boundary conditions or internal variability between the two periods. We checked this by computing instantaneous relationships between clouds and large-scale meteorology for each summer season individually. In both the model and the observations, year-to-year differences in cloud–meteorology relationships are small compared to the difference between the model and observations (not shown).

In the model simulations we use the Cloud Feedback Model Intercomparison Project Observation Simulator Package (COSP) (Bodas-Salcedo et al. 2011), which simulates satellite retrievals. We briefly describe the COSP method here, but detailed descriptions of the MODIS, CPR, and CALIOP simulators can be found in Pincus et al. (2012), Haynes et al. (2007), and Chepfer et al. (2008), respectively. At each time step and for each model column, COSP stochastically generates multiple subgrid-scale profiles called ''subcolumns'' (Klein and Jakob 1999; Webb et al. 2001). The number of subcolumns is sufficiently large to statistically represent the subgrid-scale variability, and subcolumn clouds are consistent with the model's cloud overlap assumption. Each cloudy subcolumn is then used to estimate what the CPR, CALIOP, and MODIS instruments would retrieve if they were orbiting above. Statistics of these simulated retrievals are aggregated and can be compared to similar statistics from satellite observations. The COSP satellite simulators overcome differences in scale between observations and model output and account for limitations in the observations, thus allowing for a direct statistical comparison of observations and model output.

While satellite simulators account for most limitations in satellite observations, like all models, they are imperfect. For example, satellite simulators do not account for errors in the retrieval of partly cloudy pixels, which is problematic for evaluating broken clouds. Satellite simulators are also unable to account for bias in the observations that occurs when the solar zenith angle is large, but since all sunlit scenes in the CCCM observations have solar zenith angles that are small enough to avoid the solar zenith angle bias, this limitation does not affect our analysis. Limitations of satellite simulators are discussed in detail by Pincus et al. (2012). Despite their imperfections, satellite simulators have proven useful for comparing climate model output to observations in a consistent way.

COSP variables used in this study are listed in Table 1. MODIS cloud optical depth, liquid water path, and ice water path are divided by MODIS cloud fraction to convert the gridbox-average values to in-cloud values (the average over cloudy scenes only). Using in-cloud values allows us to separate biases due to the frequency of occurrence of clouds from biases due to cloud properties when clouds are seen. Additionally, we compute albedo similarly to the CERES observations. Because the solar zenith angle is 60° or less for the sunlit scenes in the CCCM observations, model albedo is calculated only for grid points where the solar zenith angle is less than 60°.

e. *Statistical methods*

Our goal is to describe the sensitivity of clouds to variations in the four meteorological predictors mentioned above: SST, ω_{500}, EIS, and low-level temperature advection. We also use principal component analysis to identify common patterns of variability of these meteorological predictors, and we describe the sensitivity of clouds to variations in the leading principal component. Three steps are taken to prepare the data for principal component analysis. Starting with the gridded dataset of the four meteorological predictors, the seasonal cycle is removed by subtracting the monthly mean climatology. Anomalies of the meteorological fields are then linearly interpolated to the time and location of each satellite footprint. Next, the resulting meteorological fields are standardized to have unit variance and a mean of zero so that each variable contributes equally to the principal component analysis. Our use of principal component analysis is different than common practice in geophysical sciences. Principal component analysis is commonly applied to datasets that have a space and a time dimension, with the goal of finding spatial patterns in the data and how strongly they are expressed as a function of time. Here, instead of a space dimension we have a list of the four meteorological predictors, and instead of a time dimension, each entry corresponds to a different satellite footprint. Our goal is to find common patterns of the four meteorological predictors that vary across satellite footprints.

Throughout this study, we composite the cloud and radiation observations based on the various meteorological predictors and average the data. This approach illuminates the sensitivity of clouds to variations in large-scale meteorology, and, importantly, it does not assume linearity of the cloud data. For a given bin, random error of the mean is determined assuming a Gaussian distribution and computing the standard error of the mean (SE):

$$\mathrm{SE} = \frac{\sigma}{\sqrt{N}}.$$

Here, σ is the sample standard deviation and N is the effective degrees of freedom. The value N is determined using the *CloudSat* vertical feature mask (Sassen and Wang 2008), which classifies clouds into eight types based on cloud and precipitation vertical structure. In a string of consecutive satellite footprints, two neighboring footprints are considered independent only if the predominant cloud type in the two footprints is different. The 95% confidence interval for the mean, shown in the error bars throughout this study, is ±1.96SE. Note that this confidence interval does not account for systematic error in the retrievals. However, since the systematic errors in the observations are reproduced by the satellite simulators, this confidence interval can be used to test whether or not a model bias is statistically significant.

3. Results

a. *Observed linkages between clouds and large-scale meteorology*

We begin by describing the climatology of clouds and meteorology over the Southern Ocean during austral summer. Figure 1 shows the climatology of four meteorological predictor variables used in this study: ω_{500}, SST, low-level temperature advection, and EIS. Mean large-scale subsidence is seen over the subtropical oceans off the west coast of South America, Australia, and Africa, while mean large-scale ascent is seen near the southern end of South America. The gradient in SST is largest between 40° and 60°S, in the latitude band containing the Antarctic Circumpolar Current. The magnitude of low-level temperature advection is maximized near the largest SST gradients—coinciding with the storm-track regions. Estimated inversion strength is generally maximized between 40° and 60°S. Although

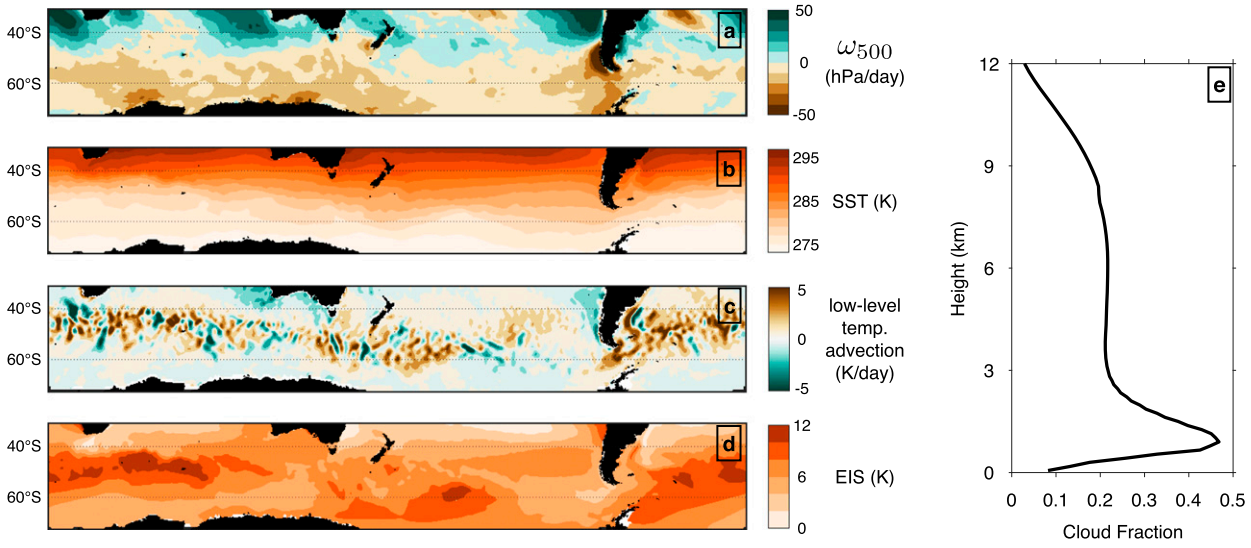

FIG. 1. Summertime climatology of (a) vertical pressure velocity at 500 hPa, (b) sea surface temperature, (c) low-level temperature advection, and (d) estimated inversion strength. (e) Vertical profile of mean cloud fraction from *CloudSat* and *CALIPSO* observations.

evidence of synoptic wave activity is seen in the low-level temperature advection map, low clouds are still much more common than middle or high clouds over the Southern Ocean (Fig. 1e).

We now describe cloud variability by compositing the data based on various meteorological predictors. Figure 2 shows cloud properties and radiation as a function of SST. Colder SST is associated with enhanced low-cloud cover, as can be seen in the vertical profile of cloud fraction. Colder SST is also associated with greater horizontal cloud fraction, greater albedo, and lower OLR. Regression coefficients for these relationships are presented in Table 2. Because SST is correlated with latitude, this figure closely resembles the zonal-mean cloud properties plotted as a function of latitude.

Figure 3 shows cloud properties and radiation as a function of ω_{500}. Deep clouds are seen during periods of strong ascent, and low clouds are seen during periods of subsidence. During periods of large-scale ascent ($\omega_{500} < 0$), horizontal cloud fraction, in-cloud optical depth, and albedo all increase with the strength of ascent. OLR decreases with stronger ascent, as stronger ascent is associated with higher cloud tops. The deepest and brightest clouds with nearly complete horizontal coverage are seen during periods of strong ascent in the midtroposphere. Same-sign, but weaker, relationships are seen during periods of subsidence: stronger subsidence is associated with smaller horizontal cloud fraction and lower albedo. Regression coefficients for both large-scale subsidence and ascent conditions are presented in Table 2.

The large-scale subsidence regime, which supports low clouds, is further explored in Fig. 4. Cloud properties are plotted as a function of EIS in Fig. 4. For weak inversions (e.g., EIS ≈ 0°C), the top of low clouds is slightly above 2 km on average. The top of the low-cloud layer becomes lower as the inversion strengthens, reaching about 1 km for very strong inversions (e.g., EIS ≈ 15°C). The in-cloud optical depth, horizontal cloud fraction, and albedo all increase with a stronger inversion. During periods of large-scale subsidence, stronger inversions are associated with low-cloud layers that are brighter, shallower, and more horizontally extensive (Table 2).

Figure 5 shows cloud properties and radiation as a function of low-level temperature advection. Like Fig. 4, only large-scale subsidence conditions are shown. Cold advection is associated with low clouds, while warm advection supports more middle and high clouds. Albedo and horizontal cloud fraction both decrease with temperature advection; strong cold-advection produces low clouds that cover about 90% of the surface and have an albedo of around 0.3, while warm advection produces clouds with smaller horizontal coverage and albedo. When both large-scale ascent and subsidence conditions are considered together, the strength of low-level temperature advection has a relatively weak influence on optical depth, albedo, and horizontal cloud fraction (not shown). This is because middle and high clouds are most common during warm advection conditions and offset the reduction in low clouds. Nonetheless, low-level temperature advection significantly influences low-cloud properties.

Some of the cloud variability in Figs. 2–5 is associated with spatial variations in the climatology of the meteorological variables, and some is associated with natural

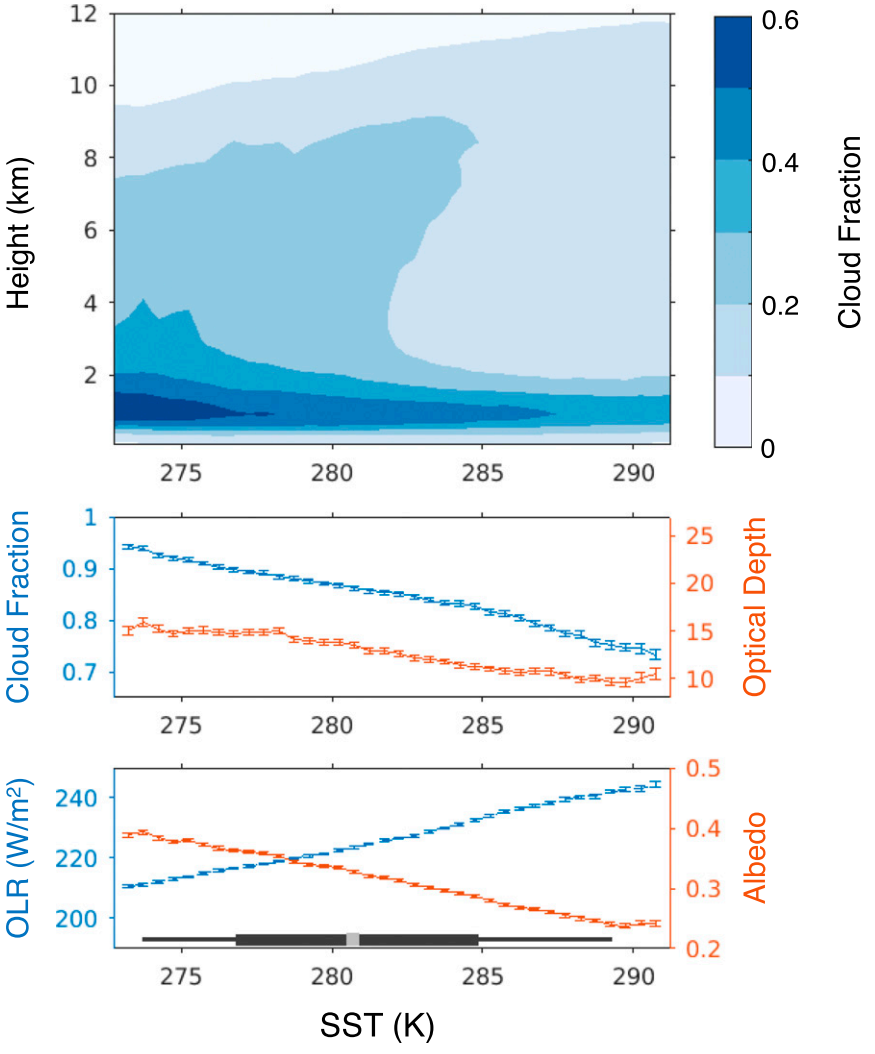

FIG. 2. Cloud properties and radiation plotted as a function of SST. (top) Vertical profile of cloud fraction observed by *CALIPSO* and *CloudSat*. (middle) Horizontal cloud fraction and in-cloud optical depth observed by MODIS. (bottom) Top-of-atmosphere outgoing LW radiation (OLR) and albedo observed by CERES. Data are binned by SST and averaged, and the error bars show the 95% confidence interval of the mean. The box plot in (bottom) shows the 5th, 25th, 50th, 75th, and 95th percentiles of SST.

variations in the meteorology. To isolate the contribution from natural variability, the climatology of cloud properties was computed on a 1° latitude by 5° longitude grid, and then the compositing was repeated with the climatology removed from the cloud and meteorology data. The relationship between cloud and SST anomalies is weak or insignificant (not shown), suggesting that most of the sensitivity of clouds to SST variations seen in Fig. 2 results from spatial variations in the climatological SST pattern. However, the weak relationship between cloud and SST anomalies could also be due to the fact that day-to-day variability in SST is relatively small. In contrast, the relationships between cloud anomalies and anomalies in low-level temperature advection, EIS, and ω_{500} are similar to those in Figs. 3–5, indicating that most of the cloud variability driven by these variables results from their natural variations.

The composites shown in Figs. 2–5 illuminate the sensitivity of Southern Ocean clouds to variations in four meteorological variables. Next we use principal component analysis to combine those four meteorological predictors into a single variable that represents a common pattern of atmospheric variability. The leading principal component (PC1), which is associated with the pattern that explains the most combined variance of the four meteorological predictors, is described in Table 3.

TABLE 2. Coefficients for cloud properties regressed on the large-scale meteorology. Uncertainty values are the 95% confidence interval for the regression coefficient. For some variables, regressions are done separately for large-scale ascent and subsidence. Two regression coefficients for OLR are not shown because they are not significantly different from zero, and one coefficient for optical depth is not shown because the data are poorly fit by a line.

	Regression coefficient			
	Cloud fraction	Optical depth	Albedo	OLR
SST	-1.10 ± 0.02 % K^{-1}	-0.37 ± 0.02 K^{-1}	-0.946 ± 0.009 % K^{-1}	2.00 ± 0.02 (W m^{-2}) K^{-1}
ω_{500}, subsidence	-6.9 ± 0.3 % (100 hPa day^{-1})$^{-1}$	-1.5 ± 0.1 (100 hPa day^{-1})$^{-1}$	-3.73 ± 0.09 % (100 hPa day^{-1})$^{-1}$	5.8 ± 0.1 (W m^{-2}) (100 hPa day^{-1})$^{-1}$
ω_{500}, ascent	-5.6 ± 0.2 % (100 hPa day^{-1})$^{-1}$	-6.1 ± 0.2 (100 hPa day^{-1})$^{-1}$	-8.0 ± 0.1 % (100 hPa day^{-1})$^{-1}$	15.7 ± 0.3 (W m^{-2}) (100 hPa day^{-1})$^{-1}$
EIS, subsidence	0.97 ± 0.03 % K^{-1}	0.12 ± 0.01 K^{-1}	0.50 ± 0.01 % K^{-1}	-
Low-level temperature advection, subsidence	-0.62 ± 0.03 % (K day^{-1})$^{-1}$	-	-0.31 ± 0.01 % (K day^{-1})$^{-1}$	-

Positive values of PC1 are associated with midtropospheric ascent, warm low-level temperature advection, and large EIS. PC1 is also uncorrelated with SST. The pattern associated with PC1 explains 37% of the combined variance of the four meteorological variables. However, because there are only four meteorological variables, and therefore only four patterns and four principal components, PC1 must explain at least 25% of the combined variance. Nonetheless, PC1 is distinct from the second principal component at the 95% confidence level according to the test proposed by North et al. (1982), so it may correspond to a ''real'' mode of atmospheric variability.

To help interpret the mode of atmospheric variability associated with PC1, vertical profiles of temperature, wind, and temperature advection are considered. Anomalies of these quantities are plotted as a function of PC1 in Fig. 6. Positive values of PC1 are associated with warm anomalies, warm advection anomalies, and poleward flow throughout the troposphere, as well as an elevated tropopause: conditions associated with the warm sector of midlatitude cyclones. Similarly, negative values of PC1 are associated with the cold sector of cyclones. Therefore, PC1 can be used as a metric for the strength of the meteorological anomalies associated with midlatitude cyclones. Compared to ω_{500} or low-level temperature advection alone, PC1 is a better overall predictor of the meteorological anomalies associated with cyclones and is therefore useful for identifying cyclones.

At first glance it may seem unusual that positive values of PC1 are associated with both large EIS and ascent in the midtroposphere. Recall that positive values of PC1 are also associated with warm advection. During warm advection events the ocean regulates the temperature of the boundary layer, causing weaker warm anomalies in the boundary layer than in the free troposphere (Fig. 6a). Since EIS is a measure of the temperature difference between the free troposphere and the boundary layer, EIS tends to be larger under warm advection than under cold advection. As a check, we repeated the principal component analysis without EIS as a predictor variable. The leading principal component is very similar with and without EIS included in the analysis (correlation of $r = 0.87$).

An example of the principal component analysis technique for identifying cyclones is shown in Fig. 7. This image shows a mature cyclone that was measured by the A-Train. The A-Train ground track transects the cyclone near its center, sampling both the warm and cold sectors in one pass. The maximum value of PC1 is around 1.9 and is found in the warm-sector, the minimum value is around -2.6 and is found in the cold-sector, and

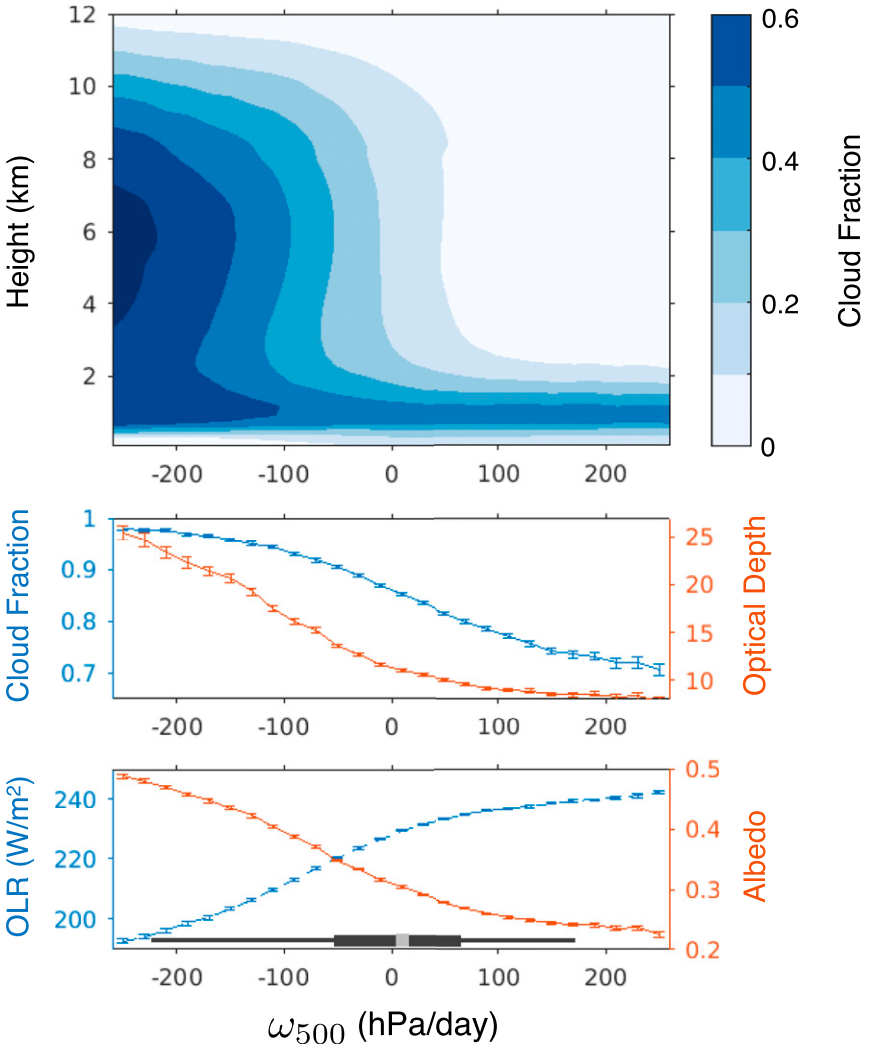

FIG. 3. Cloud properties and radiation as a function of vertical wind in the middle troposphere. (top) Vertical profile of cloud fraction observed by *CALIPSO* and *CloudSat*. (middle) Horizontal cloud fraction and in-cloud optical depth observed by MODIS. (bottom) Top-of-atmosphere OLR and albedo observed by CERES. Data are binned by ω_{500} and averaged, and the error bars show the 95% confidence interval of the mean. The box plot in (bottom) shows the 5th, 25th, 50th, 75th, and 95th percentiles of ω_{500}.

PC1 smoothly transitions between these values. It is helpful to keep this example in mind when interpreting the results that follow.

Cloud properties and radiation as a function of PC1 are shown in Fig. 8. In the cyclone warm sector (PC1 positive), clouds are deep, high topped, bright, and have horizontal coverage of 85% or more. In the cyclone cold sector (PC1 negative), low clouds with lower albedo, optical depth, and horizontal cloud fraction are seen. The strength of the cyclone, as indexed by PC1, affects cloud properties differently in the warm and the cold sectors. In the cold sector, MODIS-observed cloud fraction and optical depth and CERES-observed albedo are nearly constant for PC1 less than −1. In other words, in the cyclone cold sector, cloud properties are weakly sensitive to variations in the large-scale meteorology. In contrast to the cold sector, warm-sector clouds are much more sensitive to the strength of the meteorological anomalies.

b. *Evaluation of CAM5 and CAM5 + CLUBB*

COSP satellite simulator software allows for a direct comparison between the observations presented above and output from global climate models. We will evaluate the models based on their ability to reproduce the observed cloud properties under different meteorological

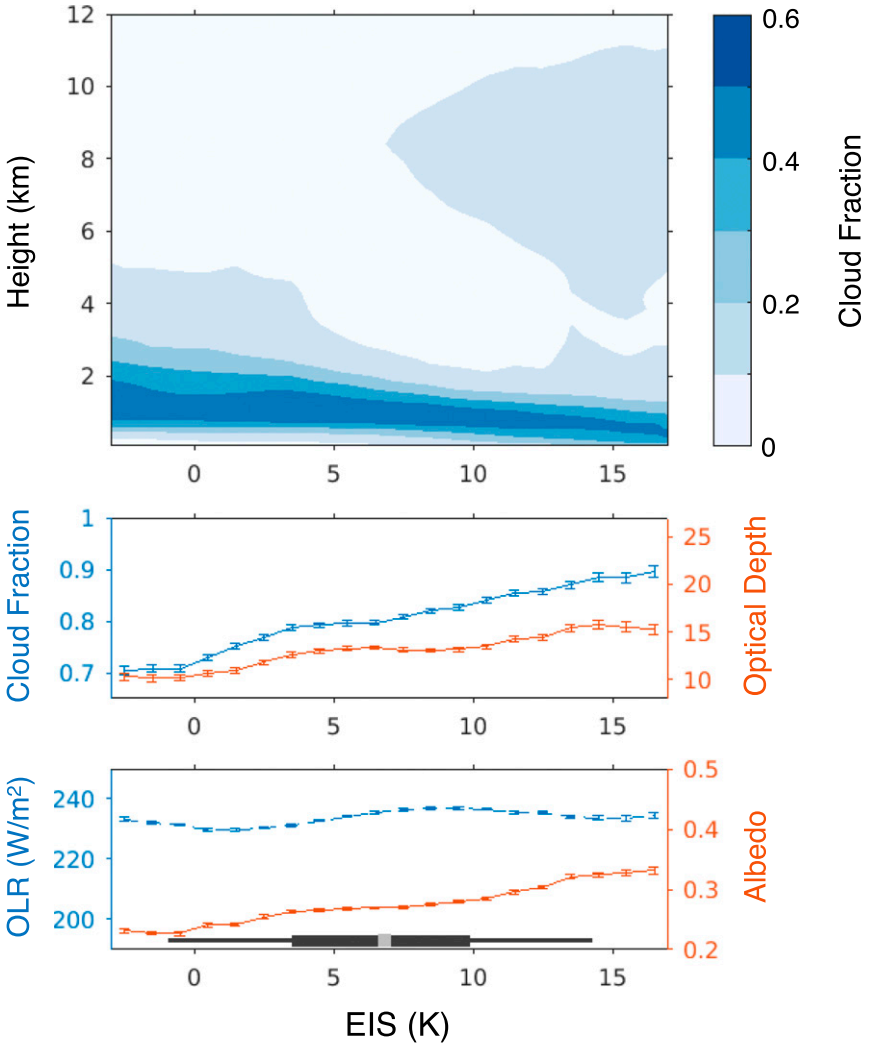

FIG. 4. Cloud properties and radiation during periods of large-scale subsidence, plotted as a function of estimated inversion strength (EIS). (top) Vertical profile of cloud fraction observed by *CALIPSO* and *CloudSat*. (middle) Horizontal cloud fraction and in-cloud optical depth observed by MODIS. (bottom) Top-of-atmosphere OLR and albedo observed by CERES. Data are binned by EIS and averaged, and the error bars show the 95% confidence interval of the mean. The box plot in (bottom) shows the 5th, 25th, 50th, 75th, and 95th percentiles of EIS.

conditions. Because model bias in absorbed SW radiation over the Southern Ocean is especially large and problematic, we focus on the summer season and evaluate cloud properties related to SW reflection.

Our evaluation includes MODIS-retrieved liquid and ice water path, but it is important to keep two things in mind when interpreting these values. First, MODIS liquid water path retrievals are highly uncertain during large-scale ascent (section 2c). These conditions are shown for completeness, but caution should be used when comparing observations to model output. Second, since the MODIS simulator is designed to capture the imperfections of the MODIS retrieval, it can produce ice water path values that are very different than those simulated by the model. The MODIS simulator identifies the cloud phase from the topmost portion of the highest clouds, and it computes optical depth from the entire column, including the contributions from liquid cloud, ice cloud, and—in this particular model—snow (Kay et al. 2012). The MODIS simulator then assumes a cloud of uniform phase and uses the optical depth value to compute the liquid or ice water path (Pincus et al. 2012). This means that if any liquid cloud is present beneath moderately thick ice cloud, then the MODIS

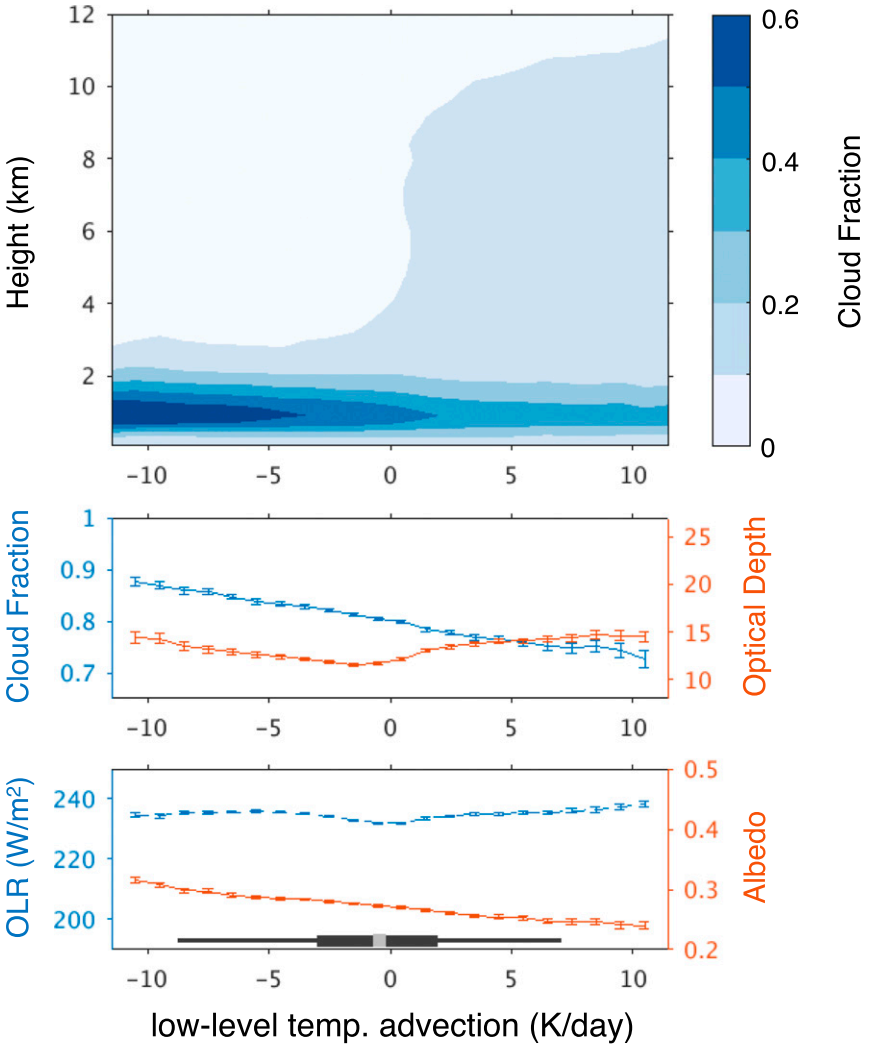

FIG. 5. Cloud properties and radiation during large-scale subsidence, plotted as a function of low-level temperature advection. (top) Vertical profile of cloud fraction observed by *CALIPSO* and *CloudSat*. (middle) Horizontal cloud fraction and in-cloud optical depth observed by MODIS. (bottom) Top-of-atmosphere OLR and albedo observed by CERES. Data are binned by low-level temperature advection and averaged, and the error bars show the 95% confidence interval of the mean. The box plot in (bottom) shows the 5th, 25th, 50th, 75th, and 95th percentiles of low-level temperature advection.

simulator will treat it as ice. The actual ice water path simulated by the models is generally less than the ice water path computed by the MODIS simulator (not shown).

Figure 9 shows observed and modeled cloud properties related to SW reflection. In the average of all scenes, albedo in CAM5 and CAM5 + CLUBB are in agreement with the observations. However, in both model configurations, MODIS-observed cloud fraction is too small, in-cloud optical depth is too large, and in-cloud liquid water path is too small. CAM5 also overestimates in-cloud ice water path. Stratifying the data by ω_{500} reveals the origin of the cloud biases. First, note that albedo in both model configurations agrees well with observations for a wide range of conditions. However, under large-scale subsidence ($\omega_{500} > 0$), both model configurations underestimate MODIS cloud fraction by around 0.1–0.3 and overestimate MODIS in-cloud optical depth by around 5. In other words, low clouds are too few and too bright. Under large-scale subsidence, in-cloud liquid and ice water path biases are dramatically reduced in CAM5 + CLUBB. The in-cloud optical depth bias in CAM5 + CLUBB appears to be the result of an underestimate of cloud droplet effective radius

TABLE 3. Description of the two leading principal components of the four meteorological predictors: ω_{500}, SST, low-level temperature advection, and EIS. The table includes the fraction of variance explained by the principal components and the correlation coefficient between the principal components and each of the four meteorological predictor variables.

Principal component	Fraction of variance explained	Correlation coefficient			
		ω_{500}	SST	Low-level temperature advection	EIS
Observations					
PC1	0.37	−0.67	−0.10	0.78	0.64
PC2	0.27	0.30	−0.88	−0.20	0.42
CAM5 + CLUBB					
PC1	0.42	−0.77	−0.14	0.83	0.61
PC2	0.27	0.29	−0.88	−0.20	0.42
CAM5					
PC1	0.41	−0.76	−0.15	0.82	0.60
PC2	0.27	0.30	−0.87	−0.20	0.44

rather than an overestimate of condensed water path (not shown). However, differences in snow properties could also play a role since snow substantially contributes to the values predicted by the MODIS simulator in CAM5 (Kay et al. 2012). Under large-scale ascent ($\omega_{500} < 0$), the cloud fraction and optical depth biases are smaller, but very large biases in cloud ice water path on the order of several hundred grams per square meter are seen. Model clouds contain far too much ice compared to observations. We also checked that these results hold for the actual liquid and ice water paths simulated by the model. When CLUBB is used, clouds contain more liquid and less ice, and the total condensed water path is slightly reduced (not shown).

Furthermore, midlatitude cyclones and their associated clouds in CAM5 and CAM5 + CLUBB can be compared to those observed in nature. To accomplish this, principal component analysis is performed on model output in a similar fashion to the analysis of the observations that is described in section 2e. The leading principal component from the modeled fields is nearly identical to the leading principal component of the observations, both in the correlation with the meteorological predictors and in the fraction of variance explained (Table 3). In both model configurations, the leading principal component is distinct from the second principal component based on the test of North et al. (1982). Therefore, PC1 can be used to separate warm- and cold-sector clouds in the model simulations in a similar fashion to the observations and thus to facilitate an evaluation of clouds in midlatitude cyclones.

Modeled and observed cloud properties stratified by PC1 are shown in Fig. 10. Figures 10a and 10b show a comparison of vertical cloud and hydrometeor occurrence from the active sensors; Fig. 10a shows the observed vertical cloud fraction, while Fig. 10b shows a crude estimate of the vertical profile of hydrometeor occurrence in CAM5. The reason for this discrepancy is that in the observations, the CPR cloud mask algorithm is applied to convert radar reflectivity into an estimate of cloud fraction, while in the model, the cloud mask algorithm is not applied to the simulated radar reflectivity. Thus, for the model data, we follow Bodas-Salcedo et al. (2011) and assume a radar reflectivity of −25 dBZ or

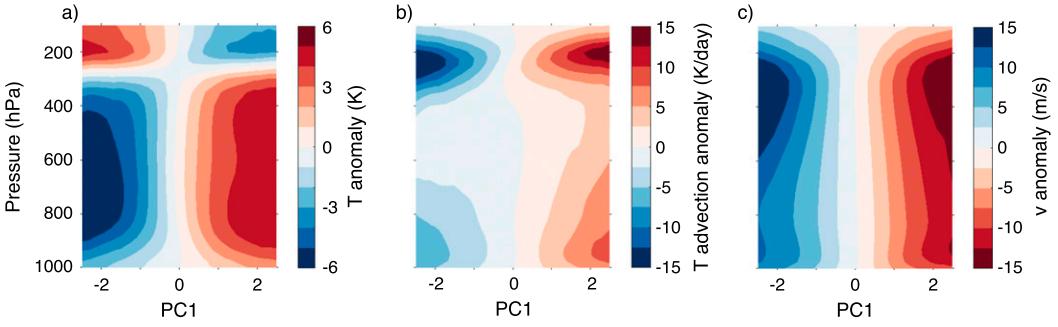

FIG. 6. Vertical profile of (a) temperature, (b) horizontal temperature advection, and (c) meridional wind anomalies plotted as a function of PC1. Note that positive values of PC1 are associated with conditions found in the warm sector of midlatitude cyclones, including warm anomalies, poleward flow, warm advection, and an elevated tropopause. Similarly, negative values of PC1 are associated with conditions found in the cold sector.

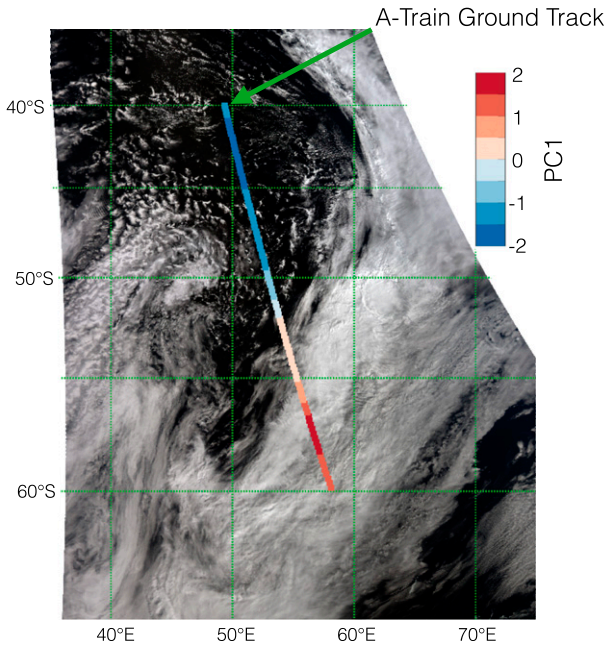

FIG. 7. Example of the cyclone identification technique. This three-color MODIS image was collected on 1045 UTC 30 December 2009. The line shows the A-Train ground track, and its color shows the value of PC1 at each location along the track.

more indicates the presence of hydrometeors as detected by the CPR. For each vertical grid box, we then estimate the hydrometeor fraction as the maximum of the CALIOP cloud fraction and the CPR hydrometeor fraction. Although Figs. 10a and 10b are not quantitatively comparable, they reveal that the vertical distribution of clouds in the cyclone warm and cold sectors are qualitatively in agreement between CAM5 and the observations. Deep and high clouds are seen in the warm sector and low clouds are seen in the cold sector, and these clouds are located at about the right elevations in CAM5.

Figures 10c–g show observed and simulated cloud properties stratified by PC1. Albedo in the model simulations is in close agreement with observations both in the warm and cold sectors of cyclones. However, compensating ''too few, too bright'' biases are pronounced in the cold sector. In CAM5, in-cloud liquid water path is underestimated in the warm sector and overestimated in the cold sector, and in-cloud ice water path is overestimated in both. The ice water path biases are especially large and can be several hundred grams per square meter. Similar liquid and ice water path biases are seen in CAM5 + CLUBB in the warm sector, but remarkable improvements are seen in the cold sector. Finally, in the cyclone cold sector in CAM5 simulations, in-cloud liquid and ice water path have a strong dependence on the strength of cold advection, which is not seen in the observations. This bias is not seen in CAM5 + CLUBB.

Generally, the use of CLUBB in CAM5 appears to greatly improve the liquid and ice water content of low clouds. It is challenging to attribute these improvements to any one part of the CLUBB scheme since CLUBB and default CAM5 have very different treatments of low clouds. However, two qualities of CLUBB are probably responsible for much of the improvement. First, since CLUBB predicts the distribution of turbulent updrafts, it can simulate a wide range of cloud regimes. This flexibility makes CLUBB well suited for modeling low clouds in the diverse meteorological conditions found over the Southern Ocean. Second, CLUBB has a more realistic treatment of the phase partitioning of condensate produced by shallow convection. In CAM5, the shallow convection scheme uses a highly simplified treatment of cloud microphysics to determine condensate phase: detrained condensate is partitioned into liquid and ice based on a simple function of temperature (Park and Bretherton 2009; Park et al. 2014). Meanwhile, in CLUBB, shallow convective clouds are coupled with the full Morrison and Gettelman (2008) cloud microphysics scheme. This is important because shallow convection is the primary source of low-cloud condensate over the Southern Ocean in CAM5, and it produces a substantial amount of ice cloud (Kay et al. 2016). Therefore, an improved treatment of phase partitioning in shallow convective clouds likely contributes to the improvements in liquid and ice water path. While other processes could also contribute to the improvement in the simulated low clouds over the Southern Ocean, these two qualities of CLUBB are likely the main sources of improvement.

c. *Our results framed in the context of the existing literature*

Many studies have used cyclone compositing techniques to achieve a process-level understanding of the relationships between clouds and large-scale meteorology (e.g., Lau and Crane 1995, 1997; Field and Wood 2007; Naud et al. 2010; Govekar et al. 2011; Catto 2016). These techniques involve compositing observations based on location with respect to the cyclone center. This approach has proven useful for separating the different cloud types and meteorological conditions found in cyclones, and it provides a broad picture of the cloud types that are problematic in climate models (Bodas-Salcedo et al. 2014). Our method achieves a similar separation of warm- and cold-sector clouds, but it also retains quantitative information about the strength of the meteorological anomalies associated with cyclones

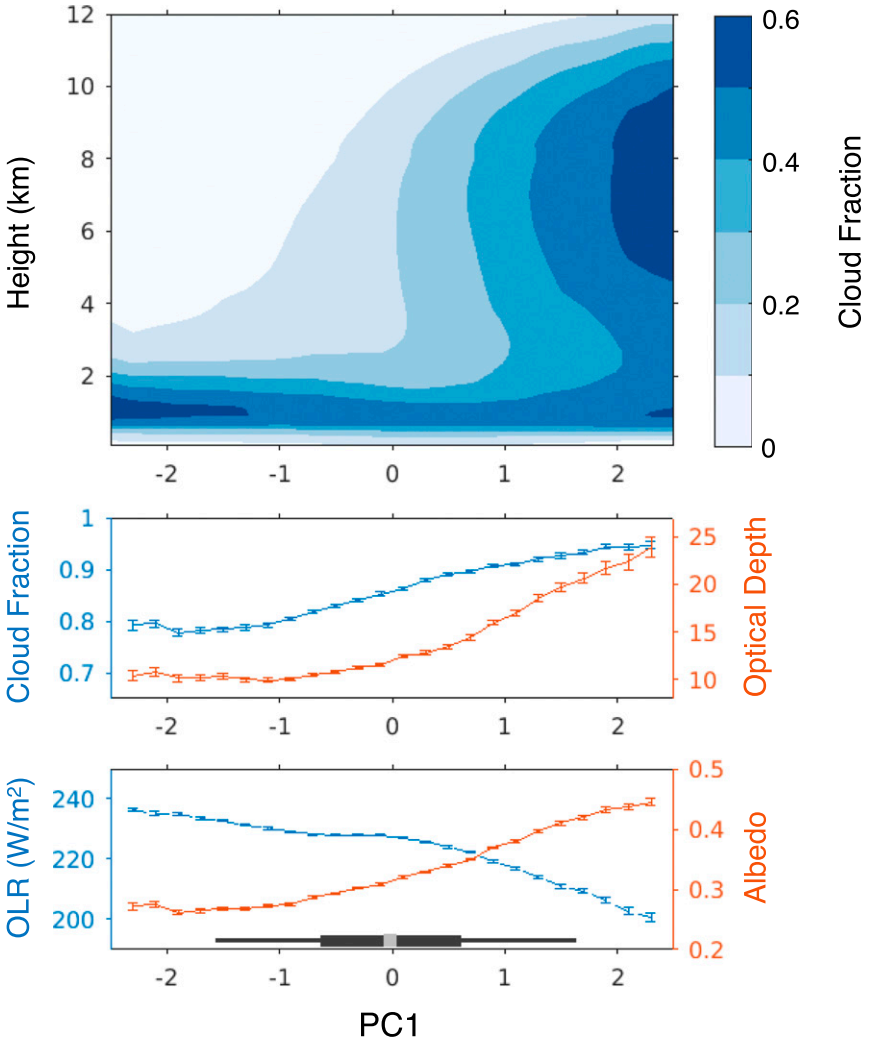

FIG. 8. Cloud properties and radiation plotted as a function of PC1, the first principal component of the four meteorological predictors. Recall that positive values of PC1 are associated with the warm sector of midlatitude cyclones, while negative values of PC1 are associated with the cold sector. (top) Vertical profile of cloud fraction observed by *CALIPSO* and *CloudSat*. (middle) Horizontal cloud fraction and in-cloud optical depth observed by MODIS. (bottom) Top-of-atmosphere OLR and albedo observed by CERES. Data are binned by PC1 and averaged, and the error bars show the 95% confidence interval of the mean. The box plot in (bottom) shows the 5th, 25th, 50th, 75th, and 95th percentiles of PC1.

and their influence on clouds. Like cyclone compositing, our method can be used to evaluate climate models. However, it provides an even more stringent test: the sensitivity of clouds to the meteorology within the different sectors of midlatitude cyclones can be evaluated.

Our results are also consistent with the findings of Norris and Iacobellis (2005). They study the North Pacific, use passive cloud observations from ISCCP and from surface observers, and conditionally sample based on midlevel vertical motion and low-level temperature advection. They find that clouds tend to be high and bright during synoptic ascent and low during synoptic subsidence. The low clouds found during synoptic subsidence are moderately bright during cold advection and have small coverage during warm advection. Observations from surface observers reveal that summertime fog is common during warm advection, while stratus, stratocumulus, and cumulus clouds are common during cold advection. Our work builds on these findings using the diverse and high-quality observations from the A-Train and demonstrates the usefulness of these relationships for climate model evaluation.

Finally, several studies have found that GCMs commonly simulate subtropical low clouds that are too few

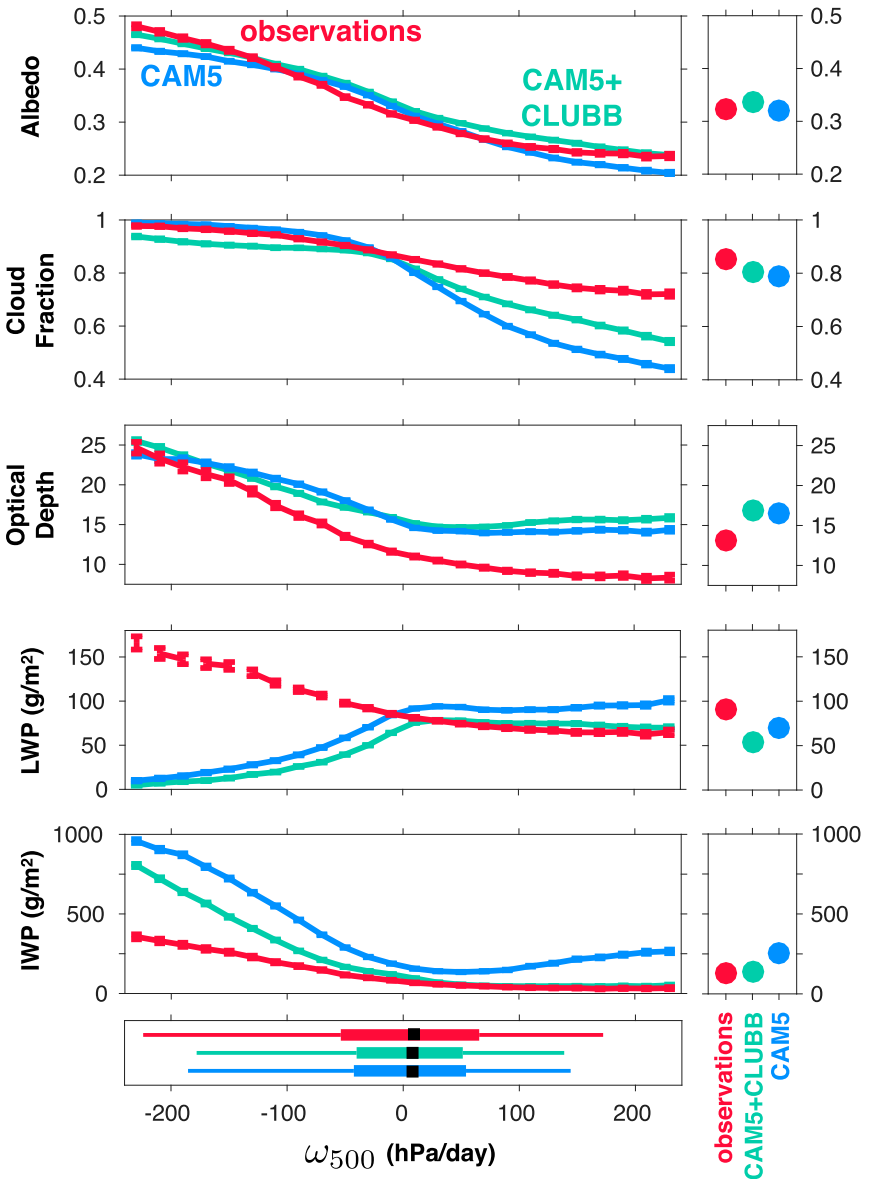

FIG. 9. Comparison of cloud properties related to SW reflection in models and observations. CERES-observed albedo and MODIS-observed cloud fraction, in-cloud optical depth, in-cloud LWP and in-cloud IWP are shown. (left) Data stratified by ω_{500}, and (right) the average of all scenes. The box plots at the bottom show the 5th, 25th, 50th, 75th, and 95th percentiles of ω_{500}. Error bars show the 95% confidence interval for the mean. In the LWP plot, a dashed line indicates conditions in which the retrieval has very large uncertainty (see section 2c).

and too bright (e.g., Weare 2004; Karlsson et al. 2008; Nam et al. 2012; Cesana and Chepfer 2012). Because low clouds in the midlatitudes are embedded within transient weather systems, their biases are more difficult to identify. We use instantaneous data to isolate low clouds over the Southern Ocean and find that they are also too few and too bright in CAM5. This result suggests that the "too few, too bright" bias could extend into the extratropics in other models as well.

4. Discussion and conclusions

In this study, relationships between cloud properties and four meteorological predictor variables over the Southern Ocean are quantified on the instantaneous time scale. Clouds are sensitive to the strength of vertical motion in the midtroposphere, and low clouds are sensitive to sea surface temperature, estimated inversion strength, and low-level temperature advection. We also examine cloud

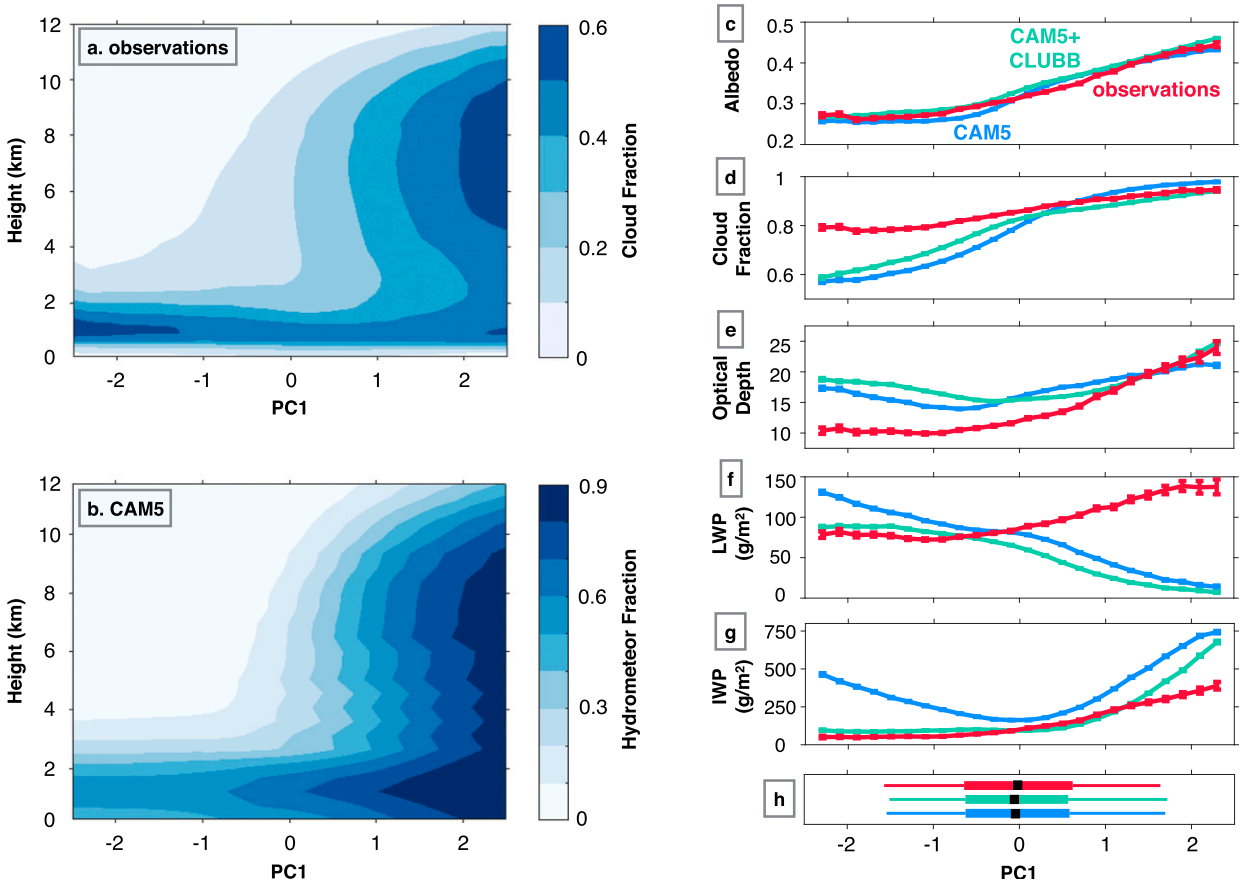

FIG. 10. Cloud properties stratified by PC1 in observations, CAM5, and CAM5 + CLUBB. Recall that positive PC1 values are associated with the warm sector of midlatitude cyclones, and negative values are associated with the cold sector. (a) Vertical profile of cloud fraction from radar and lidar observations. (b) Vertical profile of hydrometeor fraction from the radar and lidar simulators in CAM5. Note that (a) and (b) should be compared qualitatively but not quantitatively (see text). (c) Albedo and MODIS-observed (d) cloud fraction, (e) in-cloud optical depth, (f) in-cloud LWP, and (g) in-cloud IWP. (h) Box plots show the 5th, 25th, 50th, 75th, and 95th percentiles of PC1.

properties as a function of the meteorological anomalies associated with midlatitude cyclones. The deepest, brightest clouds are found in the cyclone warm sector, while low clouds with lower albedo are found in the cold sector. These observations are compared to clouds simulated by the Community Atmosphere Model, version 5, run in default configuration and coupled with the CLUBB boundary layer scheme. In default CAM5, we find that cold-sector clouds are too few and too bright, contain too much ice, and are too sensitive to the strength of meteorological anomalies. Using CLUBB substantially improves the last two biases.

The model evaluation in this study has two important implications. First, we demonstrated that instantaneous observations from the A-Train can be compared to output from global climate models with COSP satellite simulator software for a powerful evaluation of clouds in global climate models. This approach goes beyond evaluating the cloud climatology and reveals cloud biases that occur under different meteorological conditions. We also present an index that facilitates the evaluation of cyclone warm- and cold-sector clouds. This index is only useful for model evaluation if the model reasonably simulates the large-scale meteorological features of midlatitude cyclones. This is the case for CAM5, and is likely the case for other models, since midlatitude cyclones are typically well resolved in global climate models. (A typical horizontal length scale for midlatitude cyclones is on the order of several thousand kilometers—an order of magnitude larger than the typical horizontal resolution of global climate models.) It would be insightful if other modeling groups performed similar evaluations and considered regions other than the Southern Ocean.

Second, we demonstrated that the default version of CAM5 substantially overestimates in-cloud ice water path. When CLUBB is coupled with CAM5, the liquid and ice water content in low clouds is greatly

improved—probably because the flexibility of CLUBB allows it to better simulate turbulence in the diverse meteorological conditions found over the Southern Ocean and because CLUBB has a more realistic treatment of the phase partitioning of condensate formed by shallow convection. This improvement in low clouds very likely has important implications for cloud feedback simulated by the model. Many have argued that the dominant cloud feedback at midlatitudes results from warmer temperatures causing clouds to favor the liquid phase over ice. Since liquid clouds are typically more reflective than ice clouds, replacing cloud ice with liquid results in optically thicker clouds, and therefore a negative feedback (Mitchell et al. 1989; Senior and Mitchell 1993; Tsushima et al. 2006; Zelinka et al. 2012; McCoy et al. 2015; Storelvmo et al. 2015; Wall and Hartmann 2015; Ceppi et al. 2016). Overestimating the ice content of low clouds in the current climate could cause this optical depth feedback to be too negative in climate models. Indeed, in current climate models, cloud optical depth in the midlatitudes is too sensitive to temperature variations, suggesting that the optical depth feedback is likely too negative (Gordon and Klein 2014; Terai et al. 2016). Since the climatology of the liquid and ice water content of low clouds are more realistic in CAM5 + CLUBB than default CAM5, the cloud optical depth feedback in the midlatitudes in CAM5 + CLUBB is likely more realistic as well. CLUBB will probably be used in future versions of the Community Atmosphere Model, and possibly adopted by other models, so the cloud optical depth feedback in the midlatitudes could be more realistic in the next generation of global climate models.

Acknowledgments. C. J. Wall and D. L. Hartmann were supported by the Regional and Global Climate Modeling Program of the Office of Science of the U.S. Department of Energy (DE-SC0012580). P.-L. Ma acknowledges support from the U.S. Department of Energy, Office of Science (BER), Regional and Global Climate Modeling program, and internal support from the Pacific Northwest National Laboratory, which is operated for the Department of Energy by Battelle Memorial Institute under Contract DE-AC05-76RL01830. We are grateful to Jay Mace, two anonymous reviewers, and the editor (S. A. Klein) for their very helpful comments. We also thank Roger Marchand for helpful discussion and Jen Kay for guidance on running the Community Atmosphere Model with the COSP satellite simulator package.

REFERENCES

Bodas-Salcedo, A., and Coauthors, 2011: COSP: Satellite simulation software for model assessment. *Bull. Amer. Meteor. Soc.*, **92**, 1023–1043, doi:10.1175/2011BAMS2856.1.

——, and Coauthors, 2014: Origins of the solar radiation biases over the Southern Ocean in CFMIP2 models. *J. Climate*, **27**, 41–56, doi:10.1175/JCLI-D-13-00169.1.

Bogenschutz, P. A., A. Gettelman, H. Morrison, V. E. Larson, D. P. Schanen, N. R. Meyer, and C. Craig, 2012: Unified parameterization of the planetary boundary layer and shallow convection with a higher-order turbulence closure in the Community Atmosphere Model: Single-column experiments. *Geosci. Model Dev.*, **5**, 1407–1423, doi:10.5194/gmd-5-1407-2012.

——, ——, ——, ——, C. Craig, and D. P. Schanen, 2013: Higher-order turbulence closure and its impact on climate simulations in the Community Atmosphere Model. *J. Climate*, **26**, 9655–9676, doi:10.1175/JCLI-D-13-00075.1.

Boucher, O., and Coauthors, 2013: Clouds and aerosols. *Climate Change 2013: The Physical Science Basis*, T. F. Stocker et al., Eds., Cambridge University Press, 571–657.

Bretherton, C. S., and S. Park, 2009: A new moist turbulence parameterization in the Community Atmosphere Model. *J. Climate*, **22**, 3422–3448, doi:10.1175/2008JCLI2556.1.

——, and M. C. Wyant, 1997: Moisture transport, lower-tropospheric stability, and decoupling of cloud-topped boundary layers. *J. Atmos. Sci.*, **54**, 148–167, doi:10.1175/1520-0469(1997)054<0148:MTLTSA>2.0.CO;2.

Catto, J. L., 2016: Extratropical cyclone classification and its use in climate studies. *Rev. Geophys.*, **54**, 486–520, doi:10.1002/2016RG000519.

Ceppi, P., and D. L. Hartmann, 2016: Clouds and the atmospheric circulation response to warming. *J. Climate*, **29**, 783–799, doi:10.1175/JCLI-D-15-0394.1.

——, Y.-T. Hwang, D. M. W. Frierson, and D. L. Hartmann, 2012: Southern Hemisphere jet latitude biases in CMIP5 models linked to shortwave cloud forcing. *Geophys. Res. Lett.*, **39**, L19708, doi:10.1029/2012GL053115.

——, D. T. McCoy, and D. L. Hartmann, 2016: Observational evidence for a negative shortwave cloud feedback in middle to high latitudes. *Geophys. Res. Lett.*, **43**, 1331–1339, doi:10.1002/2015GL067499.

Cesana, G., and H. Chepfer, 2012: How well do climate models simulate cloud vertical structure? A comparison between CALIPSO-GOCCP satellite observations and CMIP5 models. *Geophys. Res. Lett.*, **39**, L20803, doi:10.1029/2012GL053153.

——, and Coauthors, 2016: Using in situ airborne measurements to evaluate three cloud phase products derived from CALIPSO. *J. Geophys. Res. Atmos.*, **121**, 5788–5808, doi:10.1002/2015JD024334.

Cess, R. D., and Coauthors, 1990: Intercomparison and interpretation of climate feedback processes in 19 atmospheric general circulation models. *J. Geophys. Res.*, **95**, 16 601–16 615, doi:10.1029/JD095iD10p16601.

Chepfer, H., S. Bony, D. Winker, M. Chiriaco, J.-L. Dufresne, and G. Sèze, 2008: Use of CALIPSO lidar observations to evaluate the cloudiness simulated by a climate model. *Geophys. Res. Lett.*, **35**, L15704, doi:10.1029/2008GL034207.

Corbett, J. G., and N. G. Loeb, 2015: On the relative stability of CERES reflected shortwave and MISR and MODIS visible radiance measurements during the terra satellite mission. *J. Geophys. Res. Atmos.*, **120**, 11 608–11 616, doi:10.1002/2015JD023484.

Dee, D. P., and Coauthors, 2011: The ERA-Interim reanalysis: Configuration and performance of the data assimilation system. *Quart. J. Roy. Meteor. Soc.*, **137**, 553–597, doi:10.1002/qj.828.

ECMWF, 2015: ERA-Interim project. Subset: 6-hourly, December 2006–February 2011. ECMWF, accessed 22 July 2016, http://apps.ecmwf.int/datasets/.

Field, P. R., and R. Wood, 2007: Precipitation and cloud structure in midlatitude cyclones. *J. Climate*, **20**, 233–254, doi:10.1175/JCLI3998.1.

Gates, W. L., 1992: AMIP: The Atmospheric Model Intercomparison Project. *Bull. Amer. Meteor. Soc.*, **73**, 1962–1970, doi:10.1175/1520-0477(1992)073<1962:ATAMIP>2.0.CO;2.

Golaz, J. C., V. E. Larson, and W. R. Cotton, 2002: A PDF-based model for boundary layer clouds. Part I: Method and model description. *J. Atmos. Sci.*, **59**, 3540–3551, doi:10.1175/1520-0469(2002)059<3540:APBMFB>2.0.CO;2.

Gordon, N. D., and J. R. Norris, 2010: Cluster analysis of midlatitude oceanic cloud regimes: Mean properties and temperature sensitivity. *Atmos. Chem. Phys.*, **10**, 6435–6459, doi:10.5194/acp-10-6435-2010.

——, and S. A. Klein, 2014: Low-cloud optical depth feedback in climate models. *J. Geophys. Res. Atmos.*, **119**, 6052–6065, doi:10.1002/2013JD021052.

Govekar, P. D., C. Jakob, M. J. Reeder, and J. Haynes, 2011: The three-dimensional distribution of clouds around Southern Hemisphere extratropical cyclones. *Geophys. Res. Lett.*, **38**, L21805, doi:10.1029/2011GL049091.

Grosvenor, D. P., and R. Wood, 2014: The effect of solar zenith angle on MODIS cloud optical and microphysical retrievals within marine liquid water clouds. *Atmos. Chem. Phys.*, **14**, 7291–7321, doi:10.5194/acp-14-7291-2014.

Haynes, J. M., R. T. Marchand, Z. Luo, A. Bodas-Salcedo, and G. L. Stephens, 2007: A multipurpose radar simulation package: Quickbeam. *Bull. Amer. Meteor. Soc.*, **88**, 1723–1727, doi:10.1175/BAMS-88-11-1723.

——, C. Jakob, W. B. Rossow, G. Tselioudis, and J. Brown, 2011: Major characteristics of Southern Ocean cloud regimes and their effects on the energy budget. *J. Climate*, **24**, 5061–5080, doi:10.1175/2011JCLI4052.1.

Huang, Y., S. T. Siems, M. J. Manton, D. Rosenfeld, R. Marchand, G. M. McFarquhar, and A. Protat, 2016: What is the role of sea surface temperature in modulating cloud and precipitation properties over the Southern Ocean? *J. Climate*, **29**, 7453–7476, doi:10.1175/JCLI-D-15-0768.1.

Hwang, Y.-T., and D. M. W. Frierson, 2013: Link between the double-intertropical convergence zone problem and cloud biases over the Southern Ocean. *Proc. Natl. Acad. Sci. USA*, **110**, 4935–4940, doi:10.1073/pnas.1213302110.

Jakob, C., and G. Tselioudis, 2003: Objective identification of cloud regimes in the tropical western Pacific. *Geophys. Res. Lett.*, **30**, 2082, doi:10.1029/2003GL018367.

——, ——, and T. Hume, 2005: The radiative, cloud and thermodynamic properties of the major tropical western Pacific cloud regimes. *J. Climate*, **18**, 1203–1215, doi:10.1175/JCLI3326.1.

Karlsson, J., G. Svensson, and H. Rodhe, 2008: Cloud radiative forcing of subtropical low level clouds in global models. *Climate Dyn.*, **30**, 779–788, doi:10.1007/s00382-007-0322-1.

Kato, S., and Coauthors, 2010: Variable descriptions of the A-train integrated CALIPSO, CloudSat, CERES, and MODIS merged product (CCCM or C3M). NASA, https://eosweb.larc.nasa.gov/project/ceres/readme/c3m_variables_B1_v2.pdf.

Kay, J., and Coauthors, 2012: Exposing global cloud biases in the Community Atmosphere Model (CAM) using satellite observations and their corresponding instrument simulators. *J. Climate*, **25**, 5190–5207, doi:10.1175/JCLI-D-11-00469.1.

——, C. Wall, V. Yettella, B. Medeiros, C. Hannay, P. Caldwell, and C. Bitz, 2016: Global climate impacts of fixing the Southern Ocean shortwave radiation bias in the Community Earth System Model (CESM). *J. Climate*, **29**, 4617–4636, doi:10.1175/JCLI-D-15-0358.1.

Klein, S. A., and C. Jakob, 1999: Validation and sensitivities of frontal clouds simulated by the ECMWF model. *Mon. Wea. Rev.*, **127**, 2514–2531, doi:10.1175/1520-0493(1999)127<2514:VASOFC>2.0.CO;2.

Lau, N. C., and M. W. Crane, 1995: A satellite view of the synoptic-scale organization of cloud cover in midlatitude and tropical circulation systems. *Mon. Wea. Rev.*, **123**, 1984–2006, doi:10.1175/1520-0493(1995)123<1984:ASVOTS>2.0.CO;2.

——, and ——, 1997: Comparing satellite and surface observations of cloud patterns in synoptic-scale circulation systems. *Mon. Wea. Rev.*, **125**, 3172–3189, doi:10.1175/1520-0493(1997)125<3172:CSASOO>2.0.CO;2.

Lebsock, M., and H. Su, 2014: Application of active spaceborne remote sensing for understanding biases between passive cloud water path retrievals. *J. Geophys. Res. Atmos.*, **119**, 8962–8979, doi:10.1002/2014JD021568.

Loeb, N. G., and Coauthors, 2003: Angular distribution models for top-of-atmosphere radiative flux estimation from the Clouds and the Earth's Radiant Energy System instrument on the Tropical Rainfall Measuring Mission satellite. Part II: Validation. *J. Appl. Meteor.*, **42**, 240–265, doi:10.1175/1520-0450(2003)042<0240:ADMFTO>2.0.CO;2.

——, S. Kato, K. Loukachine, and N. Manalo-Smith, 2005: Angular distribution models for top-of-atmosphere radiative flux estimation from the Clouds and the Earth's Radiant Energy System instrument on the Terra satellite. Part I: Methodology. *J. Atmos. Oceanic Technol.*, **22**, 338–351, doi:10.1175/JTECH1712.1.

——, and Coauthors, 2016: CERES CCCM, version RelB1. Subset: December 2006–February 2011. NASA Langley Research Center, accessed 22 July 2016, https://ceres.larc.nasa.gov/products.php?product=CCCM.

Marchand, R., T. Ackerman, M. Smyth, and W. B. Rossow, 2010: A review of cloud top height and optical depth histograms from MISR, ISCCP, and MODIS. *J. Geophys. Res.*, **115**, D16206, doi:10.1029/2009JD013422.

Mason, S., C. Jakob, A. Protat, and J. Delanoë, 2014: Characterizing observed midtopped cloud regimes associated with Southern Ocean shortwave radiation biases. *J. Climate*, **27**, 6189–6203, doi:10.1175/JCLI-D-14-00139.1.

McCoy, D. T., D. L. Hartmann, M. D. Zelinka, P. Ceppi, and D. P. Grosvenor, 2015: Mixed-phase cloud physics and Southern Ocean cloud feedback in climate models. *J. Geophys. Res. Atmos.*, **120**, 9539–9554, doi:10.1002/2015JD023603.

McGill, M. J., M. A. Vaughan, C. R. Trepte, W. D. Hart, D. L. Hlavka, D. M. Winker, and R. Kuehn, 2007: Airborne validation of spatial properties measured by the CALIPSO lidar. *J. Geophys. Res.*, **112**, D20201, doi:10.1029/2007JD008768.

Minnis, P., and Coauthors, 2011a: CERES edition-2 cloud property retrievals using TRMM VIRS and Terra and Aqua MODIS data—Part I: Algorithms. *IEEE Trans. Geosci. Remote Sens.*, **49**, 4374–4400, doi:10.1109/TGRS.2011.2144601.

——, and Coauthors, 2011b: CERES edition-2 cloud property retrievals using TRMM VIRS and Terra and Aqua MODIS data—Part II: Examples of average results and comparisons with other data. *IEEE Trans. Geosci. Remote Sens.*, **49**, 4401–4430, doi:10.1109/TGRS.2011.2144602.

Mitchell, J. F. B., C. A. Senior, and W. J. Ingram, 1989: CO_2 and climate—a missing feedback? *Nature*, **341**, 132–134, doi:10.1038/341132a0.

Morrison, H., and A. Gettelman, 2008: A new two-moment bulk stratiform cloud microphysics scheme in the Community

Atmosphere Model, version 3 (CAM3). Part I: Description and numerical tests. *J. Climate*, **21**, 3642–3659, doi:10.1175/2008JCLI2105.1.

Nakajima, T., and M. D. King, 1990: Determination of the optical thickness and effective particle radius of clouds from reflected solar radiation measurements. Part I: Theory. *J. Atmos. Sci.*, **47**, 1878–1893, doi:10.1175/1520-0469(1990)047<1878:DOTOTA>2.0.CO;2.

Nam, C., S. Bony, J. L. Dufresne, and H. Chepfer, 2012: The too few, too bright tropical low-cloud problem in CMIP5 models. *Geophys. Res. Lett.*, **39**, L21801, doi:10.1029/2012GL053421.

Naud, C. M., A. D. Del Genio, M. Bauer, and W. Kovari, 2010: Cloud vertical distribution across warm and cold fronts in *CloudSat*–CALIPSO data and a general circulation model. *J. Climate*, **23**, 3397–3415, doi:10.1175/2010JCLI3282.1.

Neale, R. B., and Coauthors, 2011: Description of the NCAR Community Atmosphere Model (CAM5). NCAR Tech. Note NCAR/TN-486+STR, 268 pp., http://www.cesm.ucar.edu/models/cesm1.0/cam/docs/description/cam5_desc.pdf.

Norris, J. R., and S. F. Iacobellis, 2005: North Pacific cloud feedbacks inferred from synoptic-scale dynamic and thermodynamic relationships. *J. Climate*, **18**, 4862–4878, doi:10.1175/JCLI3558.1.

North, G. R., T. L. Bell, and R. F. Cahalan, 1982: Sampling errors in the estimation of empirical orthogonal functions. *Mon. Wea. Rev.*, **110**, 699–706, doi:10.1175/1520-0493(1982)110<0699:SEITEO>2.0.CO;2.

Oreopoulos, L., and W. B. Rossow, 2011: The cloud radiative effects of International Satellite Cloud Climatology Project weather states. *J. Geophys. Res.*, **116**, D12202, doi:10.1029/2010JD015472.

Park, S., and C. S. Bretherton, 2009: The University of Washington shallow convection and moist turbulence schemes and their impact on climate simulations with the Community Atmosphere Model. *J. Climate*, **22**, 3449–3469, doi:10.1175/2008JCLI2557.1.

——, ——, and P. J. Rasch, 2014: Integrating cloud processes in the Community Atmosphere Model, version 5. *J. Climate*, **27**, 6821–6856, doi:10.1175/JCLI-D-14-00087.1.

Pincus, R., S. Platnick, S. A. Ackerman, R. S. Hemler, and R. J. Patrick Hofmann, 2012: Reconciling simulated and observed views of clouds: MODIS, ISCCP, and the limits of instrument simulators. *J. Climate*, **25**, 4699–4720, doi:10.1175/JCLI-D-11-00267.1.

Rossow, W. B., and R. A. Schiffer, 1991: ISCCP cloud data products. *Bull. Amer. Meteor. Soc.*, **72**, 2–20, doi:10.1175/1520-0477(1991)072<0002:ICDP>2.0.CO;2.

——, and ——, 1999: Advances in understanding clouds from ISCCP. *Bull. Amer. Meteor. Soc.*, **80**, 2261–2287, doi:10.1175/1520-0477(1999)080<2261:AIUCFI>2.0.CO;2.

——, G. Tselioudis, A. Polak, and C. Jakob, 2005: Tropical climate described as a distribution of weather states indicated by distinct mesoscale cloud property mixtures. *Geophys. Res. Lett.*, **32**, L21812, doi:10.1029/2005GL024584.

Sassen, K., and Z. Wang, 2008: Classifying clouds around the globe with the CloudSat radar: 1-year of results. *Geophys. Res. Lett.*, **35**, L04805, doi:10.1029/2007GL032591.

Senior, C. A., and J. F. B. Mitchell, 1993: Carbon dioxide and climate: The impact of cloud parameterization. *J. Climate*, **6**, 393–418, doi:10.1175/1520-0442(1993)006<0393:CDACTI>2.0.CO;2.

Stephens, G. L., and Coauthors, 2002: The *CloudSat* mission and the A-Train. *Bull. Amer. Meteor. Soc.*, **83**, 1771–1790, doi:10.1175/BAMS-83-12-1771.

——, and Coauthors, 2008: CloudSat mission: Performance and early science after the first year of operation. *J. Geophys. Res.*, **114**, D00A18, doi:10.1029/2008JD009982.

Storelvmo, T., I. Tan, and A. V. Korolev, 2015: Cloud phase changes induced by CO_2 warming—a powerful yet poorly constrained cloud-climate feedback. *Curr. Climate Change Rep.*, **1**, 288–296, doi:10.1007/s40641-015-0026-2.

Terai, C. R., S. A. Klein, and M. D. Zelinka, 2016: Constraining the low-cloud optical depth feedback at middle and high latitudes using satellite observations. *J. Geophys. Res. Atmos.*, **121**, 9696–9716, doi:10.1002/2016JD025233.

Trenberth, K. E., and J. T. Fasullo, 2010: Simulation of present-day and twenty-first-century energy budgets of the southern oceans. *J. Climate*, **23**, 440–454, doi:10.1175/2009JCLI3152.1.

Tsushima, Y., and Coauthors, 2006: Importance of the mixed-phase cloud distribution in the control climate for assessing the response of clouds to carbon dioxide increase: A multi-model study. *Climate Dyn.*, **27**, 113–126, doi:10.1007/s00382-006-0127-7.

Voigt, A., and T. A. Shaw, 2015: Circulation response to warming shaped by radiative changes of clouds and water vapour. *Nat. Geosci.*, **8**, 102–106, doi:10.1038/ngeo2345.

Wall, C. J., and D. L. Hartmann, 2015: On the influence of poleward jet shift on shortwave cloud feedback in global climate models. *J. Adv. Model. Earth Syst.*, **7**, 2044–2059, doi:10.1002/2015MS000520.

Warren, S. G., C. J. Hahn, J. London, R. M. Chervin, and R. L. Jenne, 1988: Global distribution of total cloud cover and cloud type amounts over the ocean. NCAR Tech. Note NCAR/TN-317+STR, 170 pp., doi:10.5065/D6QC01D1.

Weare, B., 2004: A comparison of AMIP II model cloud layer properties with ISCCP D2 estimates. *Climate Dyn.*, **22**, 281–292, doi:10.1007/s00382-003-0374-9.

Webb, M., C. Senior, S. Bony, and J. J. Morcrette, 2001: Combining ERBE and ISCCP data to assess clouds in the Hadley Centre, ECMWF and LMD atmospheric climate models. *Climate Dyn.*, **17**, 905–922, doi:10.1007/s003820100157.

Wentz, F. J., and T. Meissner, 2004: AMSR-E/Aqua L2B global swath ocean products derived from Wentz algorithm, version 2. Subset used: 1 December 2006–28 February 2007. NASA National Snow and Ice Data Center Distributed Active Archive Center, accessed 1 June 2017, doi:10.5067/AMSR-E/AE_OCEAN.002.

Wielicki, B., and Coauthors, 1996: Clouds and the Earth's Radiant Energy System (CERES): An Earth observing system experiment. *Bull. Amer. Meteor. Soc.*, **77**, 853–868, https://doi.org/10.1175/1520-0477(1996)077<0853:CATERE>2.0.CO;2.

Winker, D. M., W. H. Hunt, and M. J. McGill, 2007: Initial performance assessment of CALIOP. *Geophys. Res. Lett.*, **34**, L19803 , doi:10.1029/2007GL030135.

Wood, R., and C. S. Bretherton, 2006: On the relationship between stratiform low cloud cover and lower-tropospheric stability. *J. Climate*, **19**, 6425–6432, doi:10.1175/JCLI3988.1.

Zelinka, M. D., and D. L. Hartmann, 2012: Climate feedbacks and their implications for poleward energy flux changes in a warming climate. *J. Climate*, **25**, 608–624, doi:10.1175/JCLI-D-11-00096.1.

——, S. A. Klein, and D. L. Hartmann, 2012: Computing and partitioning cloud feedbacks using cloud property histograms. Part II: Attribution to changes in cloud amount, altitude, and optical depth. *J. Climate*, **25**, 3736–3754, doi:10.1175/JCLI-D-11-00249.1.

Zhang, G. J., and N. A. McFarlane, 1995: Sensitivity of climate simulations to the parameterization of cumulus convection in the Canadian Climate Centre General Circulation Model. *Atmos.–Ocean*, **33**, 407–446, doi:10.1080/07055900.1995.9649539.